Modeling of waves generated by a moving submerged body. Applications to underwater landslides

S.T. Grilli*, P. Watts

Ocean Engineering Department, University of Rhode Island, Narragansett, RI 02882, USA

Abstract

In this work, a boundary element model of an underwater landslide is developed. Careful gridding and time stepping techniques are demonstrated that produce highly accurate simulation results based on conservation of volume. A sensitivity analysis shows how to optimize simulation accuracy. The general techniques demonstrated herein are applicable to arbitrary moving submerged bodies. © 1999 Elsevier Science Ltd. All rights reserved.

Keywords: Modeling of waves; Moving submerged body; Underwater landslides

1. Introduction

Empirical studies of water waves generated by underwater landslides have been conducted by Wiegel [1], Iwasaki [2], Heinrich [3] and Watts [4]. All these studies considered the motion of solid blocks or boundaries. Iwasaki [5,6] conducted a wide variety of numerical studies for water waves generated by solid underwater landslides of various geometries, using the linear shallow water wave equations. Heinrich [3] performed similar studies using a finite volume discretization (VOF) of the Navier–Stokes equations; these computations agreed remarkably well with experimental results. Jiang and Lebond [7,8] developed a model of deformable underwater landslides, generating waves governed by the nonlinear shallow water wave equations. Verriere and Lenoir [9] solved a linearized velocity potential problem to describe water waves generated by perturbations around a circular island. Harbitz [10] used the linear shallow water wave equations to model the Storegga landslide as a sliding solid block generating waves. Assier Rzadkiewicz et al. [11] introduced a two-phase description of sediment motion to directly simulate an underwater landslide. Summaries of tsunamis affecting the United States coastline can be found in Refs. [12–14].

The above studies showed that surface waves generated by underwater landslides are governed by many parameters describing the landslide geometry and kinematics. Most

coastal landslides can essentially be idealized as underwater bodies sliding along a sloping bottom. In such cases, and particularly for small initial submergence of the landslide, the earlier studies showed that complex nonlinear interactions may occur between surface waves and the underwater body. One important characteristic of underwater landslides is the water runup/rundown motion induced at the shoreline. Predicting this runup is of prime importance for assessing risks and magnitude of flooding in coastal areas subjected to underwater landslides. Most earlier studies considered idealized cases and/or neglected important effects for the early stages of underwater landslides, such as the strong free surface nonlinearity. Some more realistic studies, such as Ref. [3], were based on only one simulation which precludes the many sensitivity analyses required for a comprehensive and reliable runup prediction. Hence, it is desirable to develop an efficient numerical model able to simulate, with a high level of accuracy, the strong nonlinearities occurring in this problem, due to the complex motion of an underwater body of arbitrary geometry, the generation of surface waves by body motion, and of the interactions of waves with the shoreline. This is the purpose of the present study.

Over the past 15 years numerical solutions of exact nonlinear equations for inviscid water waves, using a Boundary Integral Equation (BIE) formulation, have become increasingly successful (e.g. Refs. [15–23]). Most of the recent models are two-dimensional (although a few three-dimensional solutions have been proposed; e.g. Refs. [24,25]) and solve Fully Nonlinear Potential Flow (FNPF)

* Corresponding author. Tel.: +1-401-874-6636; fax: +1-401-874-6837.
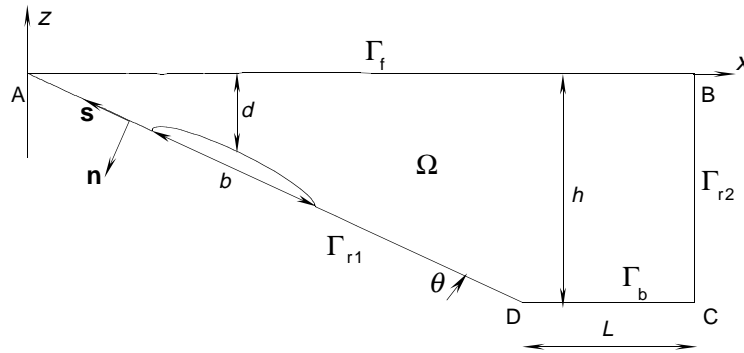 *E-mail address:* grilli@oce.uri.edu (S.T. Grilli)

Fig. 1. Sketch of NWT used in underwater landslide computations and main geometrical parameters.

equations in the physical space, using a higher-order Boundary Element Method (BEM). Waves are typically generated in such models, using wavemakers [19,26,27,40], internal sources [28,29], or other methods [26,27,30,31]. In some cases, waves are absorbed in "absorbing beaches", usually made of the combination of sponge layers and active wave absorbers [31–33]. Because of their similarity with physical wave flumes, models featuring wave generation and absorption are often referred to as *Numerical Wave Tanks* (NWT).

Grilli and coworkers [19,23,31,34] developed and refined such a NWT whose main features are (Fig. 1): (i) a higher-order BEM solution of FNPF equations in domain Ω; (ii) wave generation at the leftward extremity (Γ_{r1}; exact or approximate (using a wavemaker) finite amplitude periodic waves and solitary waves, and others); and (iii) an Absorbing Beach at the far end of the tank (featuring both free surface absorption on Γ_f and lateral active absorption on Γ_{r2}; Fig. 1). Nonlinear wave generation, propagation, runup/breaking over slopes, and interaction with coastal structures (such as submerged breakwaters) were extensively studied in this NWT [26,27,30,31,35]. More references and details about this and similar NWTs, their equations and numerical implementation, can be found in the above papers as well as in review articles by Grilli [36] and Grilli and Subramanya [37].

In the present study, Grilli et al.'s NWT is applied to the modeling of water waves generated by the motion of a submerged body, with specific application to underwater landslides. In such problems, an underwater "bump" (Fig. 1) initially sitting at rest on a sloping bottom, is gradually moved under the action of gravity. The motion is triggered by some initial perturbation (such as those created by earthquakes). Long surface waves (usually referred to as *tsunamis*) are created due to such an underwater motion and a simultaneous runup/rundown motion of the shoreline (i.e. the intersection between the water surface and the sloping bottom) occurs. In the present case, the problem is assumed to be homogeneous in the along-shore direction and, hence, to reduce to a two-dimensional problem in the vertical plane. This is usually a rather good approximation for large scale coastal landslides. In the modeling, the shape

of the bump is represented by a semi-ellipse. The law of motion of the semi-ellipse, as it starts sliding along the slope, is based on the wavemaker formalism developed by Watts [4,38] as well as the wave generation and propagation analyses given by Watts [39].

In the following we successively give, in Section 2, the representation of underwater landslides in the model, in Section 3, the model mathematical formulation and, briefly, in Section 4, its BEM numerical implementation in the NWT. Finally, in Section 5, we present applications of the model to underwater landslide, with detailed sensitivity analyses of model results accuracy as a function of numerical parameters.

2. Underwater landslide representation

In the present model, an underwater landslide is geometrically idealized by a fully submerged semi-ellipse (i.e. the "bump"), sitting on a plane slope (Fig. 1). An ellipse is chosen for its ability to represent both failure along an infinite slope of a thin landslide and failure along a circular arc of a thick landslide with the same analytical curve. The ellipse is described by the length of its base b, along the major axis, and its thickness T along its minor axis. Circular arcs of radius ϵ replace the two corners at the intersections of the ellipse and the slope. This greatly reduces or eliminates corner singularities occurring in BIE formulations (e.g. Refs. [23,34,40]). Motion of the semi-ellipse is rectilinear along the slope. Deformation of the underwater landslide is not considered in this study as Watts [4] showed that this only has a second-order effect on water wave generation.

All length scales are made dimensionless with b, time scales are made dimensionless with $\sqrt{b/g}$, and all densities are made dimensionless with ρ_0, where $g = 9.81$ m/s^2 is the acceleration of gravity and $\rho_0 = 1025$ kg/m^3 is the ambient ocean water density. For a general submerged body, the length scale b would represent a typical horizontal body length. Note, any more realistic submerged body with a known shape could easily be simulated provided sharp corners are not introduced into the domain.

A given underwater landslide is described by the slope angle θ (with slope $\tan \theta$), the landslide density ρ_ℓ, the initial submergence at the middle of the landslide d, and the length scales b, T, and ϵ (Fig. 1). The density is needed in order to specify the landslide motion. The initial submergence should satisfy, $d > 0.5b \sin \theta$ in order to ensure that the semi-ellipse is fully submerged at all times. Dimensional analysis shows that all solution characteristics are functions of the five nondimensional independent variables: $\gamma = \rho_\ell/\rho_0$, θ, d/b, T/b, and T/ϵ. This fact also holds for underwater landslide motions which can be described as approximate analytical solutions [4]:

$$s(t) = s_0 \ln \left(\cosh \frac{t}{t_0} \right) \qquad (1)$$

where s is a close approximation of center of mass motion along the slope, for solid block and deforming material underwater landslides subject to the initial conditions, $s = 0$ at $t = 0$. The center of mass velocity and acceleration at times $t > 0$ follow from the derivatives of Eq. (1):

$$\frac{\mathrm{d}s}{\mathrm{d}t}(t) = u_t \tanh \frac{t}{t_0}; \qquad \frac{\mathrm{d}^2 s}{\mathrm{d}t^2}(t) = a_0 \left(\cosh \frac{t}{t_0} \right)^{-2} \qquad (2)$$

The characteristic distance of landslide acceleration $s_0 \equiv u_t^2/a_0$, and characteristic duration of landslide acceleration $t_0 \equiv u_t/a_0$, are simple functions of initial acceleration a_0 and terminal velocity u_t. The initial acceleration is given by

$$a_0 = g \frac{\gamma - 1}{\gamma + C_m} \sin \theta \qquad (3)$$

where $C_m = 1.0$ is an approximate added mass coefficient, and the terminal velocity by

$$u_t = \sqrt{gb} \sqrt{\frac{\pi(\gamma - 1)}{2C_d} \sin \theta} \qquad (4)$$

where $C_d = 1.0$ is an approximate drag coefficient. The added mass and drag coefficients are those of a circular cylinder, since Watts [4] shows that the motion of underwater landslides with specific density $\gamma \approx 2$ is insensitive to precise values of the added mass and drag coefficients. Coulomb friction is neglected because Seed et al. [41] show that friction coefficients drop by factors between 2 and 10 following liquefaction of poorly consolidated fine sand and silt, which are common constituents at the failure planes of underwater landslides.

Estimates of the nondimensional wavelength and wave amplitude will be needed in order to discretize the simulation domain in the NWT and ensure accurate solutions of the wave generation problem. The original work of Hammack [42,43] on the scaling of (long) water wave generation and propagation is now recognized as having broad applications to wave generation by any submerged body with a significant vertical component of motion. Watts [38] introduced the "Hammack number", evaluated at time $t = t_0$ and defined as both a nondimensional time of

wave generation as well as an estimate of the nondimensional wavelength λ/b above the submerged body. To formulate the correct Hammack number for a given wave generation problem, the time scale of vertical motion t_0 is made dimensionless by the duration of long wave propagation over the body. Approximating the landslide surface by an inclined plane yields the Hammack number, $\mathbf{Ha}_0$, for this work:

$$\mathbf{Ha}_0 = \frac{\lambda}{b} = t_0\sqrt{gd} \frac{\tan \theta}{2d \left[\sqrt{1 + \dfrac{b \sin \theta}{2d}} - \sqrt{1 - \dfrac{b\sin\theta}{2d}} \right]}$$

$$\approx \frac{t_0\sqrt{gd}}{b} \qquad (5)$$

where the approximate expression on the right-hand side assumes a small θ which leads to a uniform depth d over the landslide, and is usually accurate to within $\pm 10\%$ for realistic underwater landslides. A large Hammack number, $\mathbf{Ha}_0 \gg 1$, guarantees the generation of linear water waves while underwater landslides with $\mathbf{Ha}_0 = \mathcal{O}(1)$, may display a wide range of nonlinear effects during wave generation. Water waves typically leave the wave generation region three to four times faster than the duration of landslide acceleration. In other words, $\mathbf{Ha}_0 \approx 3$ for many real events. An estimate of the maximum free surface depression above the mid-part of the initial landslide position is afforded by the semi-empirical correlation:

$$|\eta_{\max}| \approx 0.218T(\sin \theta)^{1.38} \left(\frac{b}{d} \right)^{1.25} \qquad (6)$$

derived during preliminary work appearing in Ref. [44]. This estimate is expected to be accurate to within about $\pm 30\%$ for realistic underwater landslide.

3. Mathematical formulation

A two-dimensional (2D) numerical model simulating water waves generated by an underwater landslide is developed by modifying Grilli et al.'s NWT, briefly described in the introduction. The flow is assumed to be incompressible, inviscid, and irrotational in the vertical plane. The free surface kinematics and dynamics are described by two fully nonlinear boundary conditions. The problem is solved in computational domains such as sketched in Fig. 1. Waves are generated at the leftward side and propagate into the domain. No absorbing beach is used at the extremity, which is simply assumed to be impermeable. Hence, reflection of incident waves occurs at the extremity.

Our main goal in this problem is to predict the water wave behavior near the shoreline as a function of time. Wave runup/rundown represent the most damaging terrestrial effects of landslides. Because of the small time scales involved in this problem, it is easily seen that, even in domains of rather short length, most of the interesting action

occurs at the shoreline before reflected waves have time to propagate back and affect results. Indeed, this is assured by choosing an appropriate domain size.

3.1. Governing equations and boundary conditions

Irrotational 2D flows are described by a velocity potential $\phi(\mathbf{x}, t)$, based on which the velocity field is defined as, $\mathbf{u} = \nabla\phi = (u, w)$. Continuity of mass in the fluid domain $\Omega(t)$, with boundary $\Gamma(t)$, is governed by a Laplace's equation for ϕ (Fig. 1):

$$\nabla^2\phi = 0 \qquad \text{in } \Omega(t) \tag{7}$$

Introducing the free space Green's function $G(\mathbf{x}, \mathbf{x}_l) = -(1/2\pi)\log|\mathbf{x} - \mathbf{x}_l|$, Eq. (7) transforms into a boundary integral equation (BIE)

$$\alpha(\mathbf{x}_l)\phi(\mathbf{x}_l) = \int_\Gamma \left[\frac{\partial\phi}{\partial n}(\mathbf{x})G(\mathbf{x}, \mathbf{x}_l) - \phi(\mathbf{x})\frac{\partial G(\mathbf{x}, \mathbf{x}_l)}{\partial n} \right] \mathrm{d}\Gamma \tag{8}$$

where $\mathbf{x} = (x, z)$ and $\mathbf{x}_l = (x_l, z_l)$ denote position vectors for points on the boundary, $\mathbf{n}$ is the unit outward normal vector and $\alpha(\mathbf{x}_l)$ is a geometric coefficient.

On the free surface $\Gamma_f(t)$, ϕ satisfies the kinematic and dynamic boundary conditions:

$$\frac{\mathrm{D}\mathbf{r}}{\mathrm{D}t} = \left(\frac{\partial}{\partial t} + \mathbf{u}\cdot\nabla \right)\mathbf{r} = u = \nabla\phi \qquad \text{on } \Gamma_f(t) \tag{9}$$

$$\frac{\mathrm{D}\phi}{\mathrm{D}t} = -gz + \frac{1}{2}|\nabla\phi|^2 - \frac{p_a}{\rho_0} \qquad \text{on } \Gamma_f(t) \tag{10}$$

with $\mathbf{r}$ being the position vector of a free surface fluid particle, z the vertical coordinate (positive upwards and $z = 0$ at the undisturbed free surface), and p_a the constant atmospheric pressure at the surface (simply assumed to be zero). The material derivative, which follows the motion of fluid particles, is defined by

$$\frac{\mathrm{D}}{\mathrm{D}t} \equiv \frac{\partial}{\partial t} + \mathbf{u}\cdot\nabla \tag{11}$$

The specified landslide occurs along $\Gamma_{r1}(t)$. Hence, the motion and normal velocity are prescribed over this boundary as

$$\bar{\mathbf{x}} = \mathbf{x}_\ell; \qquad \nabla\phi\cdot\mathbf{n} \equiv \frac{\overline{\partial\phi}}{\partial n} = \mathbf{u}_\ell(\mathbf{x}_\ell(t), t)\cdot\mathbf{n} \qquad \text{on } \Gamma_{r1}(t) \tag{12}$$

where $\mathbf{x}_\ell$, and $\mathbf{u}_\ell = \mathrm{d}\mathbf{x}_\ell/\mathrm{d}t$ are the landslide motion and velocity, respectively, along the landslide boundary. Note that $\mathrm{d}/\mathrm{d}t$ represents the time derivative with respect to the boundary motion.

Along the stationary bottom Γ_b and at the impermeable extremity Γ_{r2}, we have

$$\frac{\overline{\partial\phi}}{\partial n} = 0 \qquad \text{on } \Gamma_b \text{ and } \Gamma_{r2} \tag{13}$$

3.2. Time stepping

In the model, free surface boundary conditions (9) and (10) are integrated at time t, to calculate both the new geometry, $\mathbf{r}(t + \Delta t)$, and potential, $\phi(\mathbf{r}(t + \Delta t))$, on the free surface at a next time level $t + \Delta t$ (with Δt the time step). This is done using second-order Taylor series expansions:

$$\bar{\mathbf{r}}(t + \Delta t) = \mathbf{r}(t) + \Delta t\frac{\mathrm{D}\mathbf{r}}{\mathrm{D}t}(t) + \frac{(\Delta t)^2}{2}\frac{\mathrm{D}^2\mathbf{r}}{\mathrm{D}t^2}(t) + \mathcal{O}[(\Delta t)^3]$$

$$\bar{\phi}(t + \Delta t) = \phi(t) + \Delta t\frac{\mathrm{D}\phi}{\mathrm{D}t}(t) + \frac{(\Delta t)^2}{2}\frac{\mathrm{D}^2\phi}{\mathrm{D}t^2}(t) + \mathcal{O}[(\Delta t)^3] \tag{14}$$

First-order coefficients in the series are given by Eqs. (9) and (10), as a function of geometry, and ϕ and $\partial\phi/\partial n$, calculated at time t. Second-order coefficients require also knowing values of the time derivatives of both of these. The principle of time updating in the model is thus as follows. Assuming the potential is known on the free surface at time t, the continuity equation is solved in its BIE form (8), using both Eqs. (12) and (13) on the lateral and bottom boundaries, and the potential on the free surface, as boundary conditions. Based on this solution, $\partial\phi/\partial t$ is calculated on the free surface using (Bernoulli) Eq. (10). A second BIE equation is then solved, which is the time derivative of Eq. (8). To do so, specified values of $\partial\phi/\partial t$ are used as boundary conditions on the free surface, together with prescribed values of $\partial^2\phi/\partial t\partial n$ on the other boundaries. [Note that both BIEs correspond to the same boundary geometry and, hence, have the same BEM discretized form. Therefore, the solution of the second BIE only takes a small fraction of the time needed to solve the first BIE.]

For the additional boundary conditions on the bottom and extremity boundaries, we simply have from Eq. (13)

$$\frac{\overline{\partial^2\phi}}{\partial t\partial n} = 0 \qquad \text{on } \Gamma_b \text{ and } \Gamma_{r2} \tag{15}$$

The first time derivative of the second Eq. (12) provides the last boundary condition for $\partial^2\phi/\partial t\partial n$ along the moving boundary Γ_{r1}. This, however, must be carefully done due to the combination of boundary and fluid motions. Details are given in Section 3.3.

3.3. Detailed boundary condition for a submerged moving body

Consider a fully submerged rigid landslide moving along the sloping boundary Γ_{r1}, with the displacement of its center of mass, $s(t)$, given by Eq. (1) (Fig. 1). Here, the landslide motion is a simple translation parallel to the slope, but more general motions could easily be addressed.

If the flow around the body does not separate and has a sufficiently large Reynolds number, then boundary layers may be neglected and the potential flow external to the

boundary layers can be sought. This also implies that there is a *slip* condition for the tangential velocity of the potential flow around the body, whereas the flow and body velocities normal to the body are identical (as expressed by Eq. (12)). If the surface of the body is impermeable, then local surface velocities $\mathbf{u}_\ell$ and accelerations $\mathbf{a}_\ell$ of the body, which can be obtained as functions of body center of mass motion $s(t)$ and geometry, may be used to derive equations for $\partial\phi/\partial n$ and $\partial^2\phi/\partial t\partial n$. This was done for the former in Eq. (12), and is done here for the latter.

A local curvilinear coordinate system is defined to describe the body surface with a normal vector $\mathbf{n}$ pointing out of the fluid domain and a tangential vector $\mathbf{s}$ prescribing a counter-clockwise circuit about the body. [Note, the unit vector $\mathbf{s}$ is not to be confused with the distance traveled along the slope $s(t)$.] The total derivative with respect to the body motion

$$\frac{\mathrm{d}}{\mathrm{d}t} \equiv \frac{\partial}{\partial t} + \mathbf{u}_\ell \cdot \nabla \tag{16}$$

is defined at the body surface, with the vector gradient operator given by

$$\nabla \equiv \mathbf{s}\frac{1}{h_s}\frac{\partial}{\partial s} + \mathbf{n}\frac{\partial}{\partial n} \tag{17}$$

where h_s is a shape factor associated with curves of constant n. The total derivative given here operates on Eulerian fields, such as the velocity potential ϕ, that are specified in the frame of reference used to describe the local surface velocity and acceleration. The body surface velocity $\mathbf{u}_\ell$ and unit vectors $\mathbf{n}$ and $\mathbf{s}$ are Lagrangian quantities that move with this surface.

When solving the BIE Eq. (8) for the potential field ϕ, the surface of the moving body has the boundary condition given by Eq. (12), corresponding to the fluid and body normal velocities being equal, just outside of a thin boundary layer. The tangential fluid velocity is then found from the solution of the velocity potential ϕ along the surface and, in general, is different from the body tangential velocity, $\mathbf{u}_\ell \cdot \mathbf{s}$. As a result, the boundary condition for the solution of the problem for $\partial\phi/\partial t$ requires a more involved derivation. Applying Eq. (16) onto Eq. (12), we have

$$\frac{\mathrm{d}}{\mathrm{d}t}\left(\frac{\partial\phi}{\partial n}\right) = \frac{\partial^2\phi}{\partial t\partial n} + \mathbf{u}_\ell \cdot \nabla\left(\frac{\partial\phi}{\partial n}\right) \tag{18}$$

The acceleration along the moving body is defined as

$$\mathbf{a}_\ell = \frac{\mathrm{d}\mathbf{u}_\ell}{\mathrm{d}t} \tag{19}$$

Hence, the normal acceleration reads

$$\mathbf{a}_\ell \cdot \mathbf{n} = \frac{\mathrm{d}(\mathbf{u}_\ell \cdot \mathbf{n})}{\mathrm{d}t} + (\mathbf{u}_\ell \cdot \mathbf{s})\frac{\mathrm{d}\mathbf{s}}{\mathrm{d}t} \cdot \mathbf{n} + (\mathbf{u}_\ell \cdot \mathbf{n})\frac{\mathrm{d}\mathbf{n}}{\mathrm{d}t} \cdot \mathbf{n} \tag{20}$$

Introducing Eq. (12) in the left-hand-side of Eq. (18) and

using the definitions (17) and (20), we obtain

$$\frac{\partial^2\phi}{\partial t\partial n} = (\mathbf{a}_\ell \cdot \mathbf{n}) - (\mathbf{u}_\ell \cdot \mathbf{s})\frac{\mathrm{d}\mathbf{s}}{\mathrm{d}t} \cdot \mathbf{n} - (\mathbf{u}_\ell \cdot \mathbf{n})\frac{\mathrm{d}\mathbf{n}}{\mathrm{d}t} \cdot \mathbf{n}$$
$$- \mathbf{u}_\ell \cdot \left(\mathbf{s}\frac{\partial^2\phi}{\partial n\partial s} + \mathbf{n}\frac{\partial^2\phi}{\partial n^2}\right) \tag{21}$$

For rigid bodies in simple translation, time derivatives of the unit vectors $\mathbf{s}$ and $\mathbf{n}$ vanish. In Eq. (21), it is straightforward to calculate $\partial^2\phi/\partial n\partial s$ from boundary condition (12), but $\partial^2\phi/\partial n^2$ is not defined in the BEM formulation. In the local coordinate system, however, continuity Eq. (1) provides the desired substitution

$$\frac{\partial^2\phi}{\partial n^2} = -\frac{\partial^2\phi}{\partial s^2} + \frac{1}{R}\frac{\partial\phi}{\partial n} \tag{22}$$

where $\partial^2\phi/\partial s^2$ is readily computed along the surface from the solution for ϕ, and $\partial\phi/\partial n$ is known from Eq. (12). $(1/R) \equiv -(1/h_s)(\partial h_s/\partial n)$ defines the local radius of curvature and the shape factor h_s may now be set to unity. A positive radius of curvature points into the body. Hence, the underwater landslide corners have negative radii of curvature $R = -\epsilon$.

Replacing Eq. (22) by Eq. (21), we finally get

$$\frac{\partial^2\phi}{\partial t\partial n} = (\mathbf{a}_\ell \cdot \mathbf{n}) - (\mathbf{u}_\ell \cdot \mathbf{s})\frac{\partial^2\phi}{\partial s\partial n} + (\mathbf{u}_\ell \cdot \mathbf{n})\frac{\partial^2\phi}{\partial s^2} - \frac{(\mathbf{u}_\ell \cdot \mathbf{n})}{R}\frac{\partial\phi}{\partial n} \tag{23}$$

which is a scalar expression that can be evaluated in the most convenient coordinate system that describes the body motion. The velocity and acceleration components for the underwater landslide model described in Section 2 are readily calculated and will not be given here.

4. Numerical formulation

4.1. Discretization

Grilli et al.'s fully nonlinear NWT uses a higher-order BEM for solving Laplace's equation. M isoparametric elements are used on lateral and bottom boundaries (typically second-order [19]). On the free surface, M_f two-node elements are used, which combine a cubic spline representation of the geometry and a cubic representation of the field variables, within the middle segment of a four-node sliding isoparametric element (MCI elements [23]).

The BIE (3) for $(\phi, \partial\phi/\partial n)$ takes the following discretized form:

$$\alpha_l\phi_l = \sum_{j=1}^{N_\Gamma}\left\{K_{d_{lj}}\frac{\partial\phi_j}{\partial n} - K_{n_{lj}}\phi_j\right\} \tag{24}$$

in which, $l = 1, \ldots, N_\Gamma$ denotes a set of collocation nodes on

the boundary, j denotes nodal values, and

$$
\begin{aligned}
K_{d_{lj}} &= \sum_{k=1}^{M+M_f} \int_{\Gamma_\xi} N_j(\xi) G(\mathbf{x}(\xi), \mathbf{x}_l) \frac{\partial s^k}{\partial \xi}(\xi)\, d\xi \\
K_{n_{lj}} &= \sum_{k=1}^{M+M_f} \int_{\Gamma_\xi} N_j(\xi) \frac{\partial G(\mathbf{x}(\xi), \mathbf{x}_l)}{\partial n} \frac{\partial s^k}{\partial \xi}(\xi)\, d\xi
\end{aligned}
\tag{25}
$$

are BEM matrices, in which, $N_j(\xi)$ are the element shape functions, and $\partial s^k/\partial \xi$ denotes the Jacobian of the transformation from element k in the domain geometry to the reference element, of boundary Γ_ξ described by the intrinsic coordinate, $\xi \in [-1, +1]$. Expressions for both the shape functions and the Jacobians are given in Ref. [19], for isoparametric elements, and in Ref. [23], for MCI elements.

Integrals in Eq. (25) are performed by a Gauss quadrature method (typically using 10 points), for the non-singular terms, and using a similar method developed for logarithmic singularities, for the singular terms [19]. Quasi-singular integrals, which may arise for regular integrals, when the outside collocation node gets too close to the boundary, are performed by "adaptive integration" [34,40]. In this method, the number of Gauss point is adaptively increased through a binary subdivision of the reference element.

Boundary conditions are introduced in Eq. (24) and the final algebraic system is assembled by moving unknowns to the left-hand-side and keeping specified terms in the right-hand-side. The solution is simply calculated using a direct LU elimination method. Note that coefficients α_l are computed, together with the diagonal coefficients of $K_{n_{lj}}$, using the "rigid mode" method.

Sharp corners along the boundary are modeled by double-nodes, with identical coordinates but different normal directions (A–D in Fig. 1). Continuity of ϕ and $\partial\phi/\partial t$ is explicitly imposed at the double nodes, in the algebraic system (24). Extended corner conditions also specifying continuity for the velocity and its time derivatives are implemented at the intersection between the free surface and lateral boundaries [23].

4.2. Selection of domain discretization for underwater landslides

In numerical methods such as the BEM, solution accuracy typically increases with increasing node density. For a given solution accuracy, however, the numerical cost associated with matrix inversion favors minimizing the size of the simulation domain and its discretization N_Γ. In each model application to an underwater landslide, the duration of the simulation t_{max}, and associated node number per characteristic wavelength λ on the free surface, n, must be prescribed in addition to the five nondimensional variables given above.

For the applications in Section 5, the domain geometry is similar to that shown in Fig. 1. The length of the sloping bottom above the initial landslide position (in Γ_{rl}) is solely determined by d/b, T/b, and θ. The length of the sloping bottom below the initial landslide position is arbitrarily set to $1.2s(t_{max})$, in order to allow for both landslide motion and extra space for flow around the landslide to develop. Beyond the slope, a constant depth channel of depth h extends over a length $L = \sqrt{gh}\, t_{max}/2$, in order to keep long waves from reflecting off of the vertical wall at the far end of the channel and propagating back onto the slope during the simulation. Wave characteristics may be mildly dependent on the duration of the simulation since a small fraction of long wave energy is reflected back towards the slope while exiting over the toe of the slope. For a given landslide simulation, the fraction of reflected wave energy and time of arrival of reflected waves in the generation region depend on the channel depth. The magnitude of reflected energy will be shown to be negligible in a later section.

Numerical errors caused by discritization can be controlled to some extent, through careful distribution of nodes along the domain boundary. On the free surface Γ_f, in order to resolve wave runup and shorter wavelength waves induced above the landslide corner, the first distance x_c is discretized by $n + 50$ evenly spaced nodes where $x_c = (d + T\cos\theta)/\tan\theta$ is the initial horizontal location of the ellipse center. The second distance x_c has $n + 25$ nodes, with a linearly increasing node spacing that matches the node spacing on either side of this free surface segment. The remainder of the free surface has n nodes per wavelength, where typically $n > 20$. To remove shorter wavelengths, under-resolved in the discretization, every 20 time steps, the vertical position of the free surface nodes is smoothed with a second-order, centered Savitzky–Golay filter involving five nodes. The vertical boundary Γ_{r2} is discretized by 10 nodes, plus 5 nodes per unit height of h/b. The constant depth channel Γ_b is discretized by 10 nodes, plus 8 nodes per wavelength λ/b. The bottom segment of the slope on Γ_{rl} begins each simulation with n nodes per wavelength which, at later times, are evenly redistributed between the landslide and the toe of the slope. The top segment of the slope finishes a simulation with n evenly distributed nodes per wavelength, with the exception of the last seven nodes. These are placed so that the uppermost three elements along the slope match the exact length of the first three free surface elements. This arrangement optimizes the effectiveness of adaptive integration for quasi-singular integrals and increases the accuracy of wave runup and rundown calculations.

The motion of underwater landslide generates water waves on the free surface. Hence, a very accurate description of landslide geometry and kinematics, and corresponding BEM solution are necessary. To achieve this, the underwater landslide is discretized with 76 nodes, in part because its nondimensional length is always unity and realistic simulations would satisfy $T \ll b$. Each landslide corner involves 13 nodes with 9 nodes prescribing the 90° arc of radius ϵ and four nodes on the slope itself, separated by 1, 3, and 7 times the nodal spacing along the arc $\pi\epsilon/16$.

The last four nodes are placed on the incline to help shape functions transit from the interpolation of a tight circular arc to a straight surface without introducing large spurious oscillations. The landslide semi-ellipse comprises 41 nodes with 10 nodes on either side devoted to a linear transition in nodal separation from the value $\pi\epsilon/16$, at the circular arcs, to the value $b/(20\sqrt{2})$ along the top of the landslide. In general, the node density per wavelength along the top of the landslide is three to four times greater than the chosen value for the free surface.

4.3. Time stepping and global accuracy

In all applications, global accuracy is checked at each time step by calculating the relative error on mass conservation, ε_v, in the computational domain

$$\varepsilon_v = \frac{\Delta A}{A_0} = \frac{1}{A}[\int_\Gamma z \, dx - A_0] \tag{26}$$

where A_0 denotes the initial area and ΔA is the area lost or gained due to numerical errors. [Note, for 2D cases with a constant density fluid, conservation of mass becomes conservation of area in the simulation domain.]

Numerical errors in the model are function of the size (i.e. distance between nodes) and degree (i.e. quadratic, cubic, and others) of the boundary elements used in the discretization, both of which control the accuracy of the BEM solution of Laplace's equation, and of the size of the selected time step Δt, which controls the accuracy of the time stepping in the series (14). Grilli and Svendsen [40] proposed a criterion for the optimal selection of time step in the model, based on a mesh Courant number. Using this criterion, Grilli and Subramanya [23] performed a detailed analysis of accuracy for waves propagating in discretized domains having MCI elements on the free surface and quadratic isoparametric elements elsewhere (like in the present application). They showed that numerical errors on mass and energy conservation reach a minimum when the mesh Courant number, defined as

$$\mathscr{C}_0 = \sqrt{gh}\frac{\Delta t}{\Delta x} \tag{27}$$

has a value around 0.4–0.5; in which Δx denotes the minimum distance between nodes on the free surface, h is a characteristic length, and $\sqrt{gh}$ a characteristic speed for gravity waves. Accordingly, using too many small time steps may provide less accurate model results, if the grid density is not simultaneously increased on the free surface.

Applying the above results to the present applications, the initial Courant number and initial free surface node density n should be selected, and the initial time step Δt_0 found accordingly. For later times, the time step should be adjusted as

$$\Delta t = \mathscr{C}_0 \frac{\Delta|\mathbf{r}|_{\min}}{\sqrt{gd}} \tag{28}$$

where $\Delta|\mathbf{r}(t)|_{\min}$ denotes the instantaneous minimum distance between nodes on the free surface, and d is the characteristic depth above the underwater landslide.

Preliminary tests, however, showed that, everything being equal, result accuracy is also affected by the landslide motion. Indeed, based on the definition [27], the Courant number relates the distance traveled by moving events over one time step, to the grid size in the simulation domain. When water waves are generated by moving submerged bodies, then there is at least one Courant number associated with surface wave motion and another associated with body motion. Two characteristic Courant numbers can thus be written:

$$\mathscr{C}_0 = \sqrt{gd}\frac{\Delta t}{\Delta|\mathbf{r}|_{\min}} \tag{29}$$

$$\mathscr{C}_0 = u_t \frac{\Delta t \, 20\sqrt{2}}{b} \tag{30}$$

for the free surface and landslide motions, respectively. Therefore, when running a simulation, the user specifies the desired Courant number $\mathscr{C}_o$ and the initial time step Δt_o is established as the smaller value provided by Eqs. (29) and (30). At later times, the instantaneous ellipse center depth and landslide velocity are used to establish the maximum permissible time step. The channel depth is not used for the Courant number because instabilities first arise in the free surface behind the accelerating landslide, due to the small length scale of the top portion of the landslide interacting with the free surface.

4.4. Adaptive integration for underwater landslides

The motivation for adaptive integration in the BEM solution was briefly discussed above (for details, see Refs. [34,40]). In the applications, adaptive integration is used to improve solution accuracy whenever an exterior node subtends an angle greater than 45° with respect to a nearby element, or whenever large gradients in boundary values are known to occur (thus requiring increased accuracy). Either condition may be met near corners of the simulation domain. Therefore, the first two elements on either side of each double node A–D are flagged to employ adaptive integration if needed.

For underwater landslides, at the junction of the free surface and the slope, the first three elements are flagged on both sides. An underwater landslide with a shallow initial submergence d/b could have nodes on the semi-ellipse that subtend an angle greater than 45° with free surface elements and vice versa. The minimum depth $z_{\min}$ for which adaptive integration would be needed is calculated for each discretized domain, based on the free surface and landslide element lengths. The estimated wave amplitude $|\eta_{\max}|$ from Eq. (6) is then subtracted from $z_{\min}$ to ensure that adaptive integration would also be available during wave generation and propagation if needed. All elements with
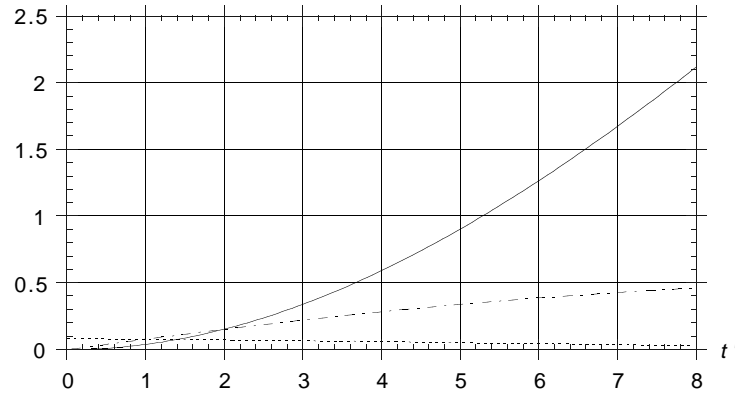
Fig. 2. Landslide motion s' (—), velocity $\mathrm{d}s'/\mathrm{d}t'$ (– – –), and acceleration $\mathrm{d}^2 s'/\mathrm{d}t'^2$ (- - - - -), for $\gamma = 1.8537$, $\theta = 15°$ and $d/b = 0.1295$ ($s'_0 = 4.4825$, $t'_0 = 7.6089$, $u'_t = 0.5891$, $a'_0 = 0.07742$).

nodes located between $0 > z > z_{\min}$ are flagged to allow for adaptive integration as are all free surface elements located above these slope and landslide elements.

5. Sensitivity analysis of solution results

We performed a sensitivity analysis of model results to numerical parameters, for underwater landslides such as sketched in Fig. 1.

5.1. Initial data and numerical parameters

All the studied landslides were specified in the model with $\gamma = 1.8537$, $\theta = 15°$, $d/b = 0.1295$, $T/\epsilon = 100$, and $T/b = 0.05176$. In this case, the initial location of the mid-part of the elliptical landslide is $x'_i = 0.683$. Using these data and applying the theory developed in Section 2 (Eqs. (1)–(5)), we have, $s'_0 = 4.4825$, $t'_0 = 7.6089$, $u'_t = 0.5891$, $a'_0 = 0.07742$, $\mathbf{Ha}_0 = \lambda' = 2.0416$, and $|\eta'_{\max}| = 0.0225$, where dashes denote nondimensional quantities and the nondimensional gravitational acceleration g' is unity. Corresponding landslide motion s', velocity $\mathrm{d}s'/\mathrm{d}t'$ and acceleration $\mathrm{d}^2 s'/\mathrm{d}t'^2$ calculated with Eqs. (1) and (2) are plotted in Fig. 2, as a function of dimensionless time t'.

We initially selected a node density $n = 30$. This density was later varied in the sensitivity analyses. Following are details of numerical parameters corresponding to $n = 30$. Based on the rules for domain geometry and discretization given before, we have $h' = 0.8605$ and $L' = 3.3527$. The total domain length at the free surface is found to be $6.5644b$. The corresponding BEM discretization has $N_\Gamma = 338$ nodes and $M_\Gamma = 252$ boundary elements, with $M_\mathrm{f} = 170$ two-node MCI elements on the free surface. The rest are three-node isoparametric elements. The initial minimum free surface node spacing is, $\Delta x'_0 = x'_\mathrm{c} \lambda'/(n x'_\mathrm{c} + 49\lambda') = 0.01138$ since the distance $x'_\mathrm{c} = 0.6699$. We first used $\mathscr{C}_0 = 0.2$, hence, based on Eq. (29), $\Delta t'_0$ is $\mathscr{C}_0 \Delta x'_0 \sqrt{b/d} = 0.00633$. The instantaneous velocity at $t' = 0$ is zero, leading to a time step infinitely larger than that

based on node spacing. The smaller of the two time steps is chosen.

We initially intended to limit computations to $t' < t'_{\max} = 0.95 t'_0 = 7.23$, because no significant water waves were generated above the initial landslide position for later times. At $t' = t'_{\max}$, the landslide has moved over a distance $s'(t'_{\max}) = 1.78$ (i.e., $1.78b$ in dimensional quantities), and its velocity reaches $\mathrm{d}s'/\mathrm{d}t' = 0.435$ or 74% of u'_t. In practice, however, the maximum number of time steps had to be limited to keep the duration of simulations and disk storage space within reasonable bounds (i.e. less than 2500 or so). Because the time step is automatically calculated by the program and can become quite small as terminal velocity is approached, computations were stopped at $t'_{\max} = 0.53 t'_0 = 4.01$. Since these slightly truncated results were able to capture the maximum free surface depression reached at x'_i, they were deemed sufficient (Fig. 4). The maximum free surface depression measured at this location provides both a characteristic wave amplitude for the simulation as well as a relevant time at which to evaluate mass conservation errors (here $t' \cong 3.6$). Fig. 3 shows three free surface profiles calculated at $t' = 0.596$, 1.134 and 1.583 and Fig. 4 shows the surface elevation calculated as a function of time at a numerical gage located at x'_i (marked as g in Fig. 3). Finally, note that the maximum free surface depression reached at x'_i is 0.02673, which is close to its estimate $|\eta'_{\max}|$, using the approximate theory of Section 2.

5.2. Assessment of model accuracy using mass conservation error

The numerical error on mass conservation, ε_v, was calculated for the initial numerical data given above, using Eq. (26), as a function of nondimensional time t'. Results are plotted in Fig. 5. [Note, computations later carried out for other geometries/discretizations indicate similar error magnitudes and trends as those given hereafter.] The shape of the (solid) error curve in the figure is very similar to s' in Fig. 2, particularly for $t' > 2$. [The dashed curve is a
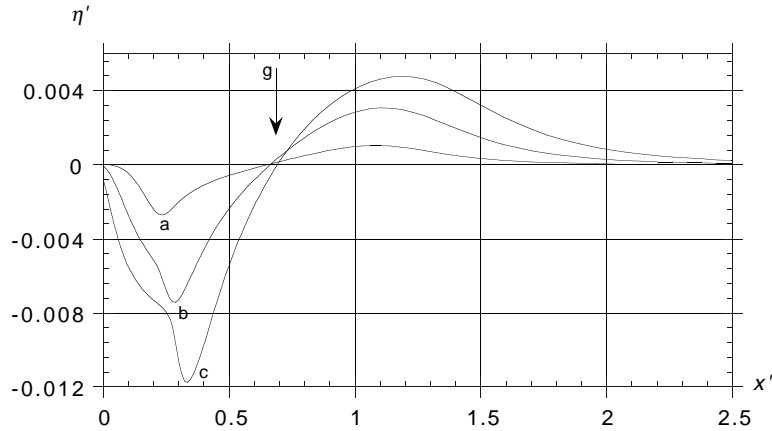
Fig. 3. Free surface profiles calculated at $t' = a$: 0.596, b: 1.134, and c: 1.583, for the landslide of characteristics given in Fig. 2.

scaling of s' by a factor 5.2510^{-5}, slightly shifted downward.] This indicates that, after the initial stages, the landslide motion is the leading cause for most of the errors in the simulations. In particular, the rate of change in simulation area appears to closely correspond to the instantaneous velocity of the underwater landslide for $t' > 2$.

Grilli and Svendsen [40] analyzed numerical errors during the initial stages of the motion of a surface peircing wavemaker and showed that impulsive starts with finite jumps in acceleration at $t = 0$ (such as in the present case with $a_0 = 0.077g$; see Fig. 2) usually lead to larger numerical errors that for more gradually accelerated wavemakers. A large initial error in mass conservation can be seen in Fig. 5. A more detailed analysis of numerical errors and sensitivity to numerical parameters is given in the following sections.

5.3. Relating mass conservation to wave amplitude

Hammack [38] and Watts [43] derived the scale of water wave amplitudes above a submerged body based on body motion and mass conservation. The same technique permits

errors in conservation of mass to be related to characteristic errors in wave amplitudes. The error in nondimensional wave amplitude is estimated as the nondimensional area lost (or gained) during a simulation divided by a single nondimensional wavelength. Since the landslide appears to be the largest source of error, changes in area would be localized around the landslide. Hence, using Eq. (26), we have

$$\frac{\Delta \eta_{\max}}{b} = \Delta \eta'_{\max} \approx \varepsilon_v \frac{A_0}{\lambda b} = \varepsilon_v \frac{A'_0}{\lambda'} \tag{31}$$

For the data given above, we have an initial domain area $A'_0 = 4.2262$ and, applying Eq. (31), $\Delta \eta'_{\max} = 0.5381 \varepsilon_v$, and $\Delta \eta'_{\max}/|\eta'_{\max}| = 23.92 \varepsilon_v$. This means that, in this case, the error on wave amplitude is at most a few hundredths of a percent and certainly small enough to derive quantitative results from these simulations. In particular, when $t' = 3.6$, we find $\varepsilon_v = 1.91910^{-5}$ and $\Delta \eta'_{\max} = 1.032610^{-5}$ or 0.04% of the observed maximum free surface depression. Note that the repeatability of the maximum free surface depression for all simulations had a
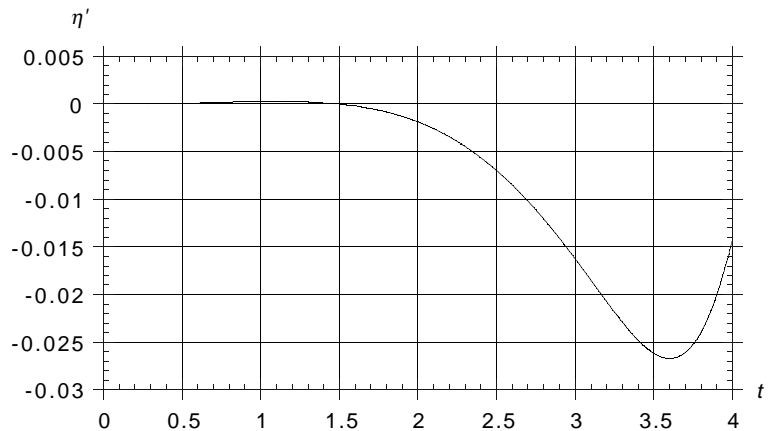

Fig. 4. Time variation of free surface elevation calculated at $x'_i = 0.683$, the initial location of the mid-part of the landslide of characteristics given in Fig. 2 (marked as g in Fig. 3).
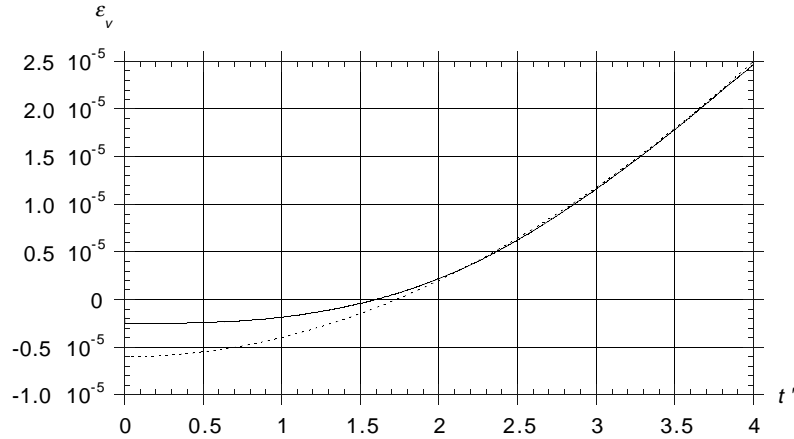
Fig. 5. Relative error ε_v on mass conservation (—) as a function of nondimensional time. (- - - - -) $-0.610^{-5} + 5.2510^{-5}s'$.

standard error of 0.5% of the mean value probably due to free surface discretization. The error due to free surface discretization is an order of magnitude larger than the error due to mass conservation.

5.4. Dependence of mass conservation on Courant number and node density

Computations were performed in the same discretization, for $\mathscr{C}_0 = 0.1$ and 0.3, by selecting an initial time step 2 times smaller and 50% larger, respectively. An optimum Courant number between that of unstable simulations and that where truncation and round-off errors dominate was not found in this work, as in Refs. [23,40]. Instead, errors seem to almost linearly decrease with C_0. [Values of ϵ_v at the time of the maximum free surface depression are 0.74, 1.92 and 3.10×10^{-5} for $\mathscr{C}_0 = 0.1$, 0.2 and 0.3, respectively.] One reason for this is that the Courant number, which is dominated by the landslide discretization (Eq. (30)), should ideally be based on the smaller nodal separation distance along the circular arcs of the landslide corners. However, these small distances would lead to prohibitively long simulations and these nodes are therefore allowed to travel many

more times their separation distance in a time step. Hence, the optimal Courant number based on node distance on the landslide semi-ellipse would be even smaller than 0.1.

Since the mass conservation error is dominated by landslide motion, this error is relatively independent of node density on the free surface beyond $n = 20$. We tried, $n = 20$, 25, 30, 35 and 40 with $\mathscr{C}_0 = 0.2$, and found an error varying by only $\pm 10\%$ at the time of the free surface minimum. This indicates that sufficient node resolution exists with $n = 30$ to accurately describe the solution.

5.5. Effect of simulation duration on water waves

The result of prime interest in these simulations of underwater landslides is the wave runup at the shoreline (point A in Fig. 1), defined as $R' = R/b$, with R the vertical shoreline motion of water during the landslide (not to be confused with radius of curvature).

Fig. 6 shows R' calculated as a function of dimensionless time, for three simulation domains based on $t'_{\max} = 0.95$, 1.25 and $1.55 t'_0$. The actual simulation times, truncated for the maximum number of time steps, are indicated in the figure caption. Virtually no difference can be observed in the
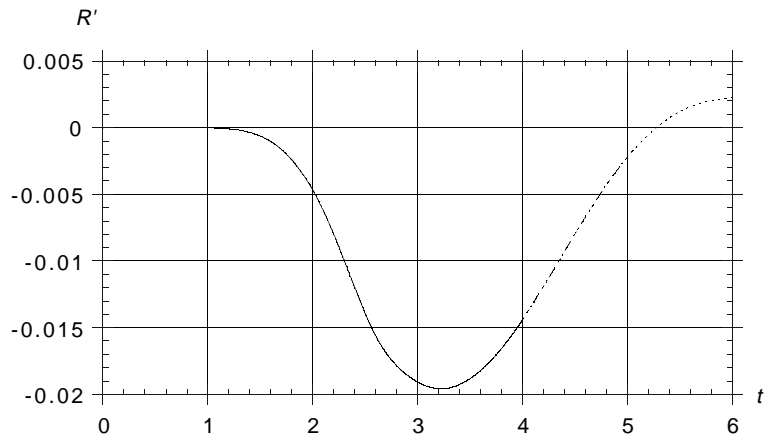

Fig. 6. Wave runup at the shore line as a function of dimensionless time for maximum durations, $t'_{\max}/t'_0 = $ (—) 0.53; (- - - - -) 0.66; (– – –) 0.79.

results for the three cases, which justifies using the smaller value of t'_{max} in computations intended to capture the free surface minimum at $x'_i = 0.683$.

Note that the maximum rundown in the figure has a value close to the estimate for the wave amplitude, $|\eta'_{max}|$.

6. Conclusions

We presented the application of a BEM, solving Fully Nonlinear Potential Flow equations, to the modeling of surface waves generated by an underwater landslide. A sensitivity analysis of the accuracy of model results to numerical parameters was conducted and showed that the rules developed for selecting spatial and temporal discretizations in the model lead to accurate results for the computed wave elevation and runup at the shoreline. Errors on the maxima of these are estimated to be at most a few tenths of a percent.

Since the discretization in a BEM is limited to the boundary, the present approach is especially efficient to address underwater landslide problems which involve two moving boundaries: the underwater body and the moving free surface, as compared to more standard domain discretization type methods. However, we prefer to emphasize that the internal flow field induced by landslide motion is properly simulated in our work. Horizontal, subsurface flows would not be captured by depth-averaged long wave models leading to the conjecture that wave generation would not be reliable. We prefer to solve an exact field equation and carefully quantify free surface errors.

We are currently conducting a sensitivity analysis of wave features by varying landslide physical parameters. These results will be presented and discussed in a forthcoming paper [44]. Comparison of numerical results with field studies will also be presented.

References

[1] Wiegel RL. Laboratory studies of gravity waves generated by the movement of a submarine body. Trans Am Geophys Union 1955;36(5):759–74.

[2] Iwasaki S. Experimental study of a tsunami generated by a horizontal motion of a sloping bottom. Bull Earth Res Inst 1982;57:239–62.

[3] Heinrich P. Nonlinear water waves generated by submarine and aerial landslides. J Waterways, Port, Coast, Ocean Engng 1992;118(3):249–66.

[4] Watts P. Water waves generated by underwater landslides. PhD thesis, California Institute of Technology, Pasadena, CA, 1997.

[5] Iwasaki S. On the estimation of a tsunami generated by a submarine landslide. Proc Intl Tsunami Symp, Vancouver, BC, 1987, p. 134–38.

[6] Iwasaki S. The wave forms and directivity of a tsunami generated by an earthquake and a landslide. Sci Tsunami Hazards 1997;15:23–40.

[7] Jiang L, Leblond PH. The coupling of a submarine slide and the surface waves which it generates. J Geophys Res 1992;97(8): 12 731–44.

[8] Jiang L, Leblond PH. Numerical modeling of an underwater Bingham plastic mudslide and the waves which it generates. J Geophys Res 1993;98(C6):10 303–17.

[9] Verriere M, Lenoir M. Computation of waves generated by submarine landslides. Intl J Num Methods Fluids 1992;14:403–21.

[10] Harbitz CB. Model simulations of tsunamis generated by the Storegga slides. Marine Geol 1992;105:1–21.

[11] Assier Rzadkiewicz S, Mariotti C, Heinrich P. Numerical simulation of submarine landslides and their hydraulic effects. J Waterways, Port, Coast, Ocean Engng 1997;123(4):149–57.

[12] Lander JF, Lockridge PA. United States Tsunamis 1890–1988. Publication 41-2, Nat. Geophysical Data Ctr., Nat. Envir. Satellite, Data, and Info. Service, Nat. Oceanic and Atmospheric Admin., US, Dept. of Commerce, Boulder, CO, 1989.

[13] Lander JF, Lockridge PA, Kozuch MJ. Tsunamis Affecting the West Coast of the United States 1806–1992. Publication 29, Nat. Geophysical Data Ctr., Nat. Envir. Satellite, Data, and Info. Service, Nat. Oceanic and Atmospheric Admin., US, Dept. of Commerce, Boulder, CO, 1993.

[14] Lander JF. Tsunamis affecting Alaska 1737–1996. Publication 31, Nat. Geophysical Data Ctr., Nat. Envir. Satellite, Data, and Info. Service, Nat. Oceanic and Atmospheric Administration, US, Dept. of Commerce, Boulder, CO, 1996.

[15] Vinje T, Brevig P. Numerical simulation of breaking waves. Adv Water Resources 1981;4:77–82.

[16] Nakayama T. Boundary element analysis of nonlinear water wave problems. Intl J Numer Methods Engng 1983;19:953–70.

[17] Dold JW, Peregrine DH. Steep unsteady water waves: an efficient computational scheme. Proc 19th Intl Conf on Coast Engineering, Houston, USA (ICCE19), 1984, p. 955–67.

[18] Dommermuth DG, Yue DKP. Numerical simulation of nonlinear axisymmetric flows with a free surface. J Fluid Mech 1987; 178:195–219.

[19] Grilli ST, Skourup J, Svendsen IA. An efficient boundary element method for nonlinear water waves. Engng Anal Boundary Elements 1989;6(2):97–107.

[20] Cointe R. numerical simulation of a wave channel. Engng Anal Boundary Elements 1990;7(4):167–77.

[21] Cooker MJ. A boundary-integral method for water wave motion over irregular bed. Engng Anal Boundary Elements 1990;7(4):205–13.

[22] Ohyama T, Nadaoka K. Development of a numerical wave tank for analysis of nonlinear and irregular wave fields. Fluid Dynam Res 1991;8:231–51.

[23] Grilli ST, Subramanya R. Numerical modeling of wave breaking induced by fixed or moving boundaries. Comput Mech 1996;17:374–91.

[24] Romate JE. The numerical simulation of nonlinear gravity waves in three dimensions using a higher order panel method. PhD dissertation, Delft Hydraulics, The Netherlands, 1989.

[25] Broeze J. Numerical modelling of nonlinear free surface waves with a 3D panel method. PhD dissertation, Enschede, The Netherlands, 1993.

[26] Grilli ST, Losada MA, Martin F. Characteristics of solitary wave breaking induced by breakwaters. J Waterways, Port, Coast, Ocean Engng 1994;120(1):74–92.

[27] Grilli ST, Subramanya R, Svendsen IA, Veeramony J. Shoaling of solitary waves on plane beaches. J Waterways, Port, Coast, Ocean Engng 1994;120(6):609–28.

[28] Brorsen M, Larsen J. Source generation of nonlinear gravity waves with the boundary integral method. Coastal Engng 1987;11:93–113.

[29] Ohyama T, Nadaoka K. Transformation of a nonlinear wave train passing over a submerged shelf without breaking. Coastal Engng 1994;24:1–22.

[30] Grilli ST, Svendsen IA, Subramanya R. Breaking criterion and characteristics for solitary waves on plane beaches. J Waterways, Port, Coast, Ocean Engng. 1997;123(3):102–12.

[31] Grilli ST, Horrillo J. Numerical generation and absorption of fully nonlinear periodic waves. J Engng Mech 1997;123(10):1060–9.

[32] Larsen J, Dancy H. Open boundaries in short wave simulations—a new approach. Coastal Engng 1983;7:285–97.

[33] Clément A. Coupling of two absorbing boundary conditions for 2D time-domain simulations of free surface gravity waves. J Comput Phys 1996;126:139–51.

[34] Grilli ST, Subramanya R. Quasi-singular integrals in the modeling of nonlinear water waves in shallow water. Engng Anal Boundary Elements 1994;13(2):181–91.

[35] Svendsen IA, Grilli ST. Nonlinear waves on steep slopes. J Coastal Res 1990;SI7:185–202.

[36] Grilli ST. Modeling of nonlinear wave motion in shallow water. In: Wrobel LC, Brebbia CA, editors. Computational methods for free and moving boundary problems in heat and fluid flow, London, UK: Comput. Mech. Pub., Elsevier Applied Sciences, 1993. p. 37–65, chap 3.

[37] Grilli ST, Subramanya R. Recent advances in the BEM modelling of nonlinear water waves. In: Power H, editor. Boundary element applications in fluid mechanics, Advances in fluid mechanics series, Southampton, UK: Comput. Mech. Publication, 1995. p. 91–122, chap 4.

[38] Watts P. Wavemaker curves for tsunamis generated by underwater landslides. J Waterways, Port, Coast, Ocean Engng 1998;12(3):127–37.

[39] Watts P. Tsunami features of solid block underwater landslides. J Waterways, Port, Coast, Ocean Engng, accepted for publication.

[40] Grilli ST, Svendsen IA. Corner problems and global accuracy in the boundary element solution of nonlinear wave flows. Engng Anal Boundary Elements 1990;7(4):178–95.

[41] Seed HB, Seed RB, Schlosser F, Blondeau F, Juran I. The landslide at the Port of Nice on October 16, 1979. Rep. No. UCB/EERC-88/10, Earthquake Engineering Research Center, University of California, Berkeley, CA, 1988.

[42] Hammack JL. Tsunamis: a model of their generation and propagation. PhD thesis, California Institute of Technology, Pasadena, CA, 1972.

[43] Hammack JL. A note on tsunamis: their generation and propagation in an ocean of uniform depth. J Fluid Mech 1973;60:769–99.

[44] Watts P, Grilli ST, Synolakis CE. Tsunami generation and run-up due to underwater landslides. In preparation.